Journal of Materials Chemistry A

Materials for energy and sustainability

Accepted Manuscript

This article can be cited before page numbers have been issued, to do this please use: R. Shepard, S. Brennan, T. R. Juran, J. Young and M. Smeu, *J. Mater. Chem. A*, 2022, DOI: 10.1039/D2TA03938A.



This is an Accepted Manuscript, which has been through the Royal Society of Chemistry peer review process and has been accepted for publication.

Accepted Manuscripts are published online shortly after acceptance, before technical editing, formatting and proof reading. Using this free service, authors can make their results available to the community, in citable form, before we publish the edited article. We will replace this Accepted Manuscript with the edited and formatted Advance Article as soon as it is available.

You can find more information about Accepted Manuscripts in the <u>Information for Authors</u>.

Please note that technical editing may introduce minor changes to the text and/or graphics, which may alter content. The journal's standard <u>Terms & Conditions</u> and the <u>Ethical guidelines</u> still apply. In no event shall the Royal Society of Chemistry be held responsible for any errors or omissions in this Accepted Manuscript or any consequences arising from the use of any information it contains.



View Article Online DOI: 10.1039/D2TA03938A

Journal Name

ARTICLE TYPE

Cite this: DOI: 00.0000/xxxxxxxxxx

Ab initio determination of a simultaneous dual-ion charging mechanism for Ni $_{0.25}$ Mn $_{0.75}$ O $_2$ through redox reactions of Ni $^{2+}$ /Ni $^{4+}$ and O $^{2-}$ /O $^{-\dagger}$

Robert Shepard, a,b Scott Brennan, Taylor Juran, Joshua Young, a,c and Manuel Smeua,*

Received Date Accepted Date

Published on 27 July 2022. Downloaded on 8/31/2022 3:59:13 AM

DOI: 00.0000/xxxxxxxxxx

Over recent years, great efforts have been made to push the limits of layered transition metal oxides for secondary battery cathodes. This is particularly true for overall capacity, which has reached a terminal theoretical value for many materials. One avenue for increasing this capacity during charging is the intercalation of anions post cation deintercalation. This work investigates the charging mechanism of the P3-Na_{0.5}Ni_{0.25}Mn_{0.75}O₂ cathode material through cation (Na) deintercalation and anion (ClO₄) intercalation by means of density functional theory. The calculations corroborate experimental findings of increased capacity (135 mAh g⁻¹ to 180 mAh g⁻¹) through the intercalation of anions. However, this work demonstrates that a process of simultaneous cation deintercalation/anion intercalation is the primary charging mechanism, with charge compensation reactions of Ni²⁺/Ni⁴⁺ and O²⁻/O⁻ occurring within the cathode material. To elucidate this simultaneous process, a novel method for computationally determining anion voltage in which one must consider full electrolyte interactions is proposed. Based on the results, it is believed that a simultaneous cation deintercalation/anion intercalation mechanism provides one potential avenue for the discovery of the next generation of secondary batteries.

1 Introduction

The Li ion battery (LIB) ^{1–7} has long been held as the industry standard for powering portable electronics ⁸. While it is believed that LIBs will never completely be replaced, many studies into alternative secondary batteries have been undertaken ^{8–16}. To start, investigation into Na would be prudent; the monovalent nature of both ions, abundance of Na, and similar chemical/electronic properties between Li and Na would make it a great choice ^{17,18}. Although Na mimics Li in many aspects, advancement of Na ion batteries (NIBs) is not without adversity.

Many materials have shown the ability to act as a cathode for NIBs, such as various oxides (*i.e.*, layered, olivine, and spinel), phosphates, and chalcogenides $^{15,16,19-23}$. These materials have been shown to possess the ability to reach 4.5 V and obtain 300 mAh g⁻¹ in various studies 24 and references therein. However, such performance is rare; on average, NIBs fail to outperform

Recently, an experimental study by Li *et al.* ²⁵ investigated the layered transition metal oxide (TMO) P3-Na_{0.5}Ni_{0.25}Mn_{0.75}O₂ for use as a Na ion battery (NIB) cathode. They found that after extracting all Na ions, ClO₄ would intercalate, thereby increasing capacity beyond what is theoretically predicted for Na ion participation alone. Specifically, they obtained a final capacity of 180 mAh g⁻¹ (a ~34% increase over the all-Na theoretical capacity of 134 mAh g⁻¹), which corresponds to an overall voltage of 4.15 V when charging their system. Furthermore, Li *et al.* proposed a multi-step process for cycling Ni_{0.25}Mn_{0.75}O₂ during which Ni species undergo a reversible cationic redox reaction (Ni²⁺ \leftrightarrow Ni⁴⁺) and O atoms undergo a reversible anionic redox reaction (O²⁻ \leftrightarrow O⁻).

To the best of the authors' knowledge, only two other computational studies have investigated ClO₄ intercalation. However, these works investigated intercalation into graphite, with the focus of their calculations solely on the physical and electronic structure changes during intercalation; no electrochemical performance was determined through density functional theory

the industry standard of 3.7 V and 372 mAh $\rm g^{-1}$ of LIBs. That is, of course, unless we go beyond the performance achieved with full extraction/intercalation of sodium. This raises the question on how one could continue further if all ions have been extracted. The answer lies with anions; the process of deintercalating cations is electronically equivalent to intercalating anions.

^a Department of Physics, Binghamton University - SUNY, 4400 Vestal Parkway East, Binghamton, NY 13902, United States.

b Department of Mathematics and Technology, Alvernia University, 400 Saint Bernardine Street, Reading, PA 19607, United States.

^c Department of Chemical and Materials Engineering, New Jersey Institute of Technology, 323 Dr. Martin Luther King Jr. Boulevard, Newark, NJ 07102, United States.

^{*} Corresponding author: msmeu@binghamton.edu

[†] Electronic Supplementary Information (ESI) available: [details of any supplementary information available should be included here]. See DOI: 00.0000/00000000.

(DFT) 26,27 . Additionally, several studies can be found with ClO₄ present in various electrolytes, again focusing on physical and electronic properties and not electrochemical performance $^{28-31}$. The work presented here will involve both intercalation within the Ni_{0.25}Mn_{0.75}O₂ cathode and the ion-electrolyte interactions present within a realistic system.

2 Computaional Methods

2.1 Computational details

In this work we investigate the processes of Na deintercalation and ClO₄ intercalation within the layered TMO of P3-Ni_{0.25}Mn_{0.75}O₂ (referred to simply as NMO hereafter) when paired with a Na metal anode and propylene carbonate (PC) electrolyte, by means of computational modeling based in DFT ^{32–38}. To accomplish this, physical structures, density of states (DOS), cell voltages, diffusion barriers, and charge analyses are all calculated with various forms of the exchange-correlation (xc) functional and van der Waals (vdW) correction schemes. Specifically, the generalized gradient approximation (GGA) by Perdew, Burke, and Ernzerhof (PBE) 39 and the strongly constrained and appropriately normed (SCAN) 40 functionals, and the DFT-D3 41 and rVV1042,43 vdW corrections were used. In addition, the rotationally invariant approach to the Hubbard U correction, as introduced by Dudarev et al. 44,45, was employed in conjunction with the PBE-D3 xc functional-vdW correction combination to accurately account for the on-site Coulomb interactions of transition metal (TM) 3(d) electrons. This combination was utilized only in electronic structure calculations revolving around the investigation of computationally demonstrating the charge compensation redox reactions of NMO (see Sec. 3.4), with values of U=4.0 eV for Mn and 6.0 eV for Ni. The decision to utilize the Hubbard U correction only for the investigations of redox reactions was based on previous computational investigations 46-50 which demonstrated its effectiveness in describing TMOs.

DFT calculations were performed using the Vienna Ab initio Simulation Package (VASP)⁵¹, which utilizes a plane wave basis set in the expansion of the Kohn-Sham single particle wave functions. The ion-electron interactions were approximated using the projector augmented wave (PAW) potentials 52 with nonspherical contributions from gradient corrections inside the PAW spheres included. Both the kinetic energy cutoff and Γ -centered Monkhorst-Pack 53 k-point grid were tested independently for convergence against a 1-meV/atom threshold. It was determined that a 700-eV kinetic energy cutoff and a $3 \times 3 \times 1$ k-point grid were sufficient for the NMO unit cell (shown in Fig. 1). Appropriate smearing methods were used for sampling the Brillouin zone for intercalated and empty NMO structures, including the Methfessel-Paxton⁵⁴ method. For electronic structure investigations (i.e., DOS), the previous methods and the tetrahedron method with Blöchl corrections 55 were utilized. All structural relaxations and energy calculations were performed using the conjugate-gradient algorithm⁵⁶ with the inclusion of electron spin (i.e., spin polarization). The ground state configuration was considered reached upon net forces on atoms falling below 0.01 eV/Å. Each system was modeled and analyzed using the Vi-

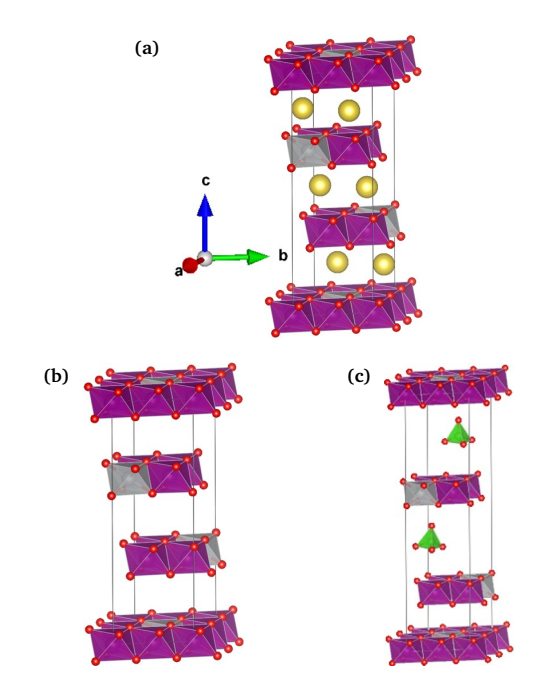


Fig. 1 The $R\bar{3}m$ unit cells of (a) Na_{0.5}Ni_{0.25}Mn_{0.75}O₂, (b) Ni_{0.25}Mn_{0.75}O₂, and (c) Ni_{0.25}Mn_{0.75}O₂(ClO₄)_{0.167} used in this work. As the discharged cathode (*i.e.*, Na_{0.5}Ni_{0.25}Mn_{0.75}O₂) was synthesized in the P3 phase²⁵, such a structure was used for the empty and ClO₄-intercalated systems. Nickel atoms are shown in gray, manganese in purple, and oxygen in red. NOTE: The three panels are not to scale.

sualization for Electronic and STructural Analysis (VESTA) software 57 .

2.2 Relaxations

Full structural relaxations (including lattice vectors) were completed on empty and cation/anion-intercalated NMO structures (see Fig. 1) using the PBE, PBE-D3, PBE-D3+U, SCAN and SCAN-rVV10 xc-vdW approximations, as mentioned in Sec. 2.1. Concentrations between x=0.083 and x=0.5, inclusive, were used for simulating intercalation of Na in Na_xNMO. These concentrations correspond to 1 and 6 ions, respectively, in our simulation cells. Additionally, x=0.5 is referred to as the "fully sodiated" concentration hereafter.

For the intercalation of ClO_4 , concentrations of y=0.083 and y=0.167 (i.e., 1 and 2 molecules, repsectively) in NMO(ClO_4) $_y$ were investigated. Intercalation of ClO_4 was halted at y=0.167 (referred to as "fully perchlorated" hereafter) based on the previously reported percentage increase in overall capacity as compared to that obtained from full desodiation 25 . Ion intercalation was completed via a series of independent site testing, the details of which are discussed in Sec. S1 & S2†.

2.3 Nudged Elastic Band

Ion migration in NMO was investigated for both Na and ClO₄, individually, using the nudged elastic band (NEB) method $^{58-65}$ with PBE-D3. The migration pathways investigated (shown in Fig. 3a & 3b) were based on the results of the site testing discussed in Sec. S1 & S2 † . To simulate ion migration, a $2\times2\times1$ su-

percell was created to allow each NEB pathway to start and end at an equivalent site (*i.e.*, the lowest energy position of a single Na or ${\rm ClO_4}$) and to create sufficient distance (*i.e.*, ~ 10 Å) between repeated images to greatly reduce any interactions between them. Unique pathways were individually tested and combined in such a way to show ion migration throughout the NMO interlayer space. The use of this method allowed migration of both Na and ${\rm ClO_4}$ along similar, although not identical, pathways. A total of 7 images were used to sample along each migration pathway.

2.4 Ab initio Molecular Dynamics

To determine the energies of our electrolyte systems, we performed *ab initio* molecular dynamics (AIMD) $^{66-69}$ simulations. To simulate the electrolyte, AIMD calculations were completed on a simulation cell consisting of 24 PC molecules and 0, 1, 2, or 3 NaClO₄ units (shown in Fig. S3†), all of which were randomly distributed throughout the simulation cell. For each system containing NaClO₄ salt, the proximity of Na to ClO₄ was investigated (including both contact and solvent-separated ion pairs) and each system was designed to correspond to densities previously reported for NaClO₄ in PC based on molarity (both explicitly determined by, and interpolated from, experiment) 70,71 . Molarity and density data for these systems are provided in Table S1†.

The AIMD simulations were run at 350 K with 1-fs time steps using the canonical (NVT) ensemble $^{72-77}$. First, each system was equilibrated for 5 ps; following this, an additional 2 ps of simulation time was performed. Frozen images were taken from each 2-ps simulation in increments of 0.1 ps and the total energy of each was computed self-consistently. The final total energy was then taken through two methods; 1) as the average of these 20 image energies and 2) an average of the entire 2-ps AIMD trajectory. For all AIMD calculations, only the Γ k-point was used and vdW interactions were included via the Grimme D3 approach 41 (i.e., PBE-D3).

2.5 Voltage

Published on 27 July 2022. Downloaded on 8/31/2022 3:59:13 AM

Once all relaxation and AIMD energies are obtained, voltage can then be calculated. In previous computational works, it has been demonstrated that the average voltage for a secondary battery can be calculated as

$$V = \frac{-\Delta G}{nF},\tag{1}$$

where ΔG is the difference in Gibbs free energy between the charged and discharged states, n is the number of electrons transferred during intercalation, and F is Faraday's constant ^{78–84}. Although ΔG can explicitly be calculated, we approximate it as equal to the internal energy (*i.e.*, DFT determined ground state energy) for this work. This approximation is expected not only to save on the overall computational costs for this investigation, but to be accurate (*i.e.*, within 0.2 V of the "true" voltage ^{78,82,84}) as well.

The approximation above allows Eqn. 1 to be rewritten in the general form of,

$$V = \frac{E_{\text{charged}} - E_{\text{discharged}}}{\text{# of e}^{-} \text{ transferred}},$$
 (2)

where $E_{\rm charged}$ is the sum of energies of the components in the charged state and $E_{\rm discharged}$ is the sum of energies of the components in the discharged state. When intercalating cations, Eqn. 2 becomes,

$$V = \frac{(E_y + (x - y)E_{\text{metal}}) - E_x}{(x - y)Z},$$
(3)

where E_y and E_x are the energies of NMO intercalated with y and x cations (where x>y), respectively, $E_{\rm metal}$ is the energy per atom of the pure cation-metal anode, and Z is the valency of the intercalated cation (Z=1 for Na). To ensure conformity to thermodynamic principles, Eqn. 3 is only applied to those cation intercalation concentrations residing on a convex hull of formation energies 15,16 . When intercalating anions, however, Eqn. 3 is no longer applicable due to the intercalated ion (ClO₄ in this work) not having a solid metal counterpart. Here, we revisit Eqn. 2 and expand based on a novel approach developed in part from previous computational work which also investigated anion voltage $^{85-90}$.

In the present work, we begin our anion voltage calculations by considering the Na metal anode, ClO_4 -intercalated cathode, and electrolyte with lower molarity of salt as components of the charged state (see Fig. 2c). The components of the discharged state (with respect to ClO_4) are then an electrolyte with a higher molarity of salt and the empty NMO structure (see Fig. 2b). This is represented mathematically by Eqn. 4 and shown schematically in Fig. 2.

In Eqn. 4, the first, second, and fifth terms are all found as described in Sec. 2.2, where $E_{\rm Na}$ is the energy per atom of the pure Na metal anode, $E_{\rm NMO,(x-y)ClO_4}$ is the energy of NMO intercalated with (x-y) (where x>y) ClO₄ molecules, and $E_{\rm NMO}$ is the energy of the empty NMO structure. The third and fourth terms in Eqn. 4 represent the PC electrolyte with y and x salt pairs, respectively. This equation was utilized to simulate charging from the empty NMO structure to the fully perchlorated one, as originally proposed by Li *et al.* 25 . However, as discussed in Sec. 3.3, Eqn. 4 will require modification to accommodate a novel charging mechanism proposed by this work.

To the best of the authors' knowledge, only four other groups have reported on the computation of anionic voltages. However, many of these other works did not model a true representation of the electrolyte with salt; they employed a molecular species model $^{85-89}$. One group did simulate such a realistic electrolyte model of salt in solvent, but their work did not involve a change in molarity of salt but a change in anionic species from AlCl_4^- to $\mathrm{Al}_2\mathrm{Cl}_7^{-90}$.

$$V = \frac{((x-y)E_{\text{Na}} + E_{\text{NMO},(x-y)\text{ClO}_4} + E_{24\text{PC},y\text{NaClO}_4}) - (E_{24\text{PC},x\text{NaClO}_4} + E_{\text{NMO}})}{(x-y)e^-}$$
(4)



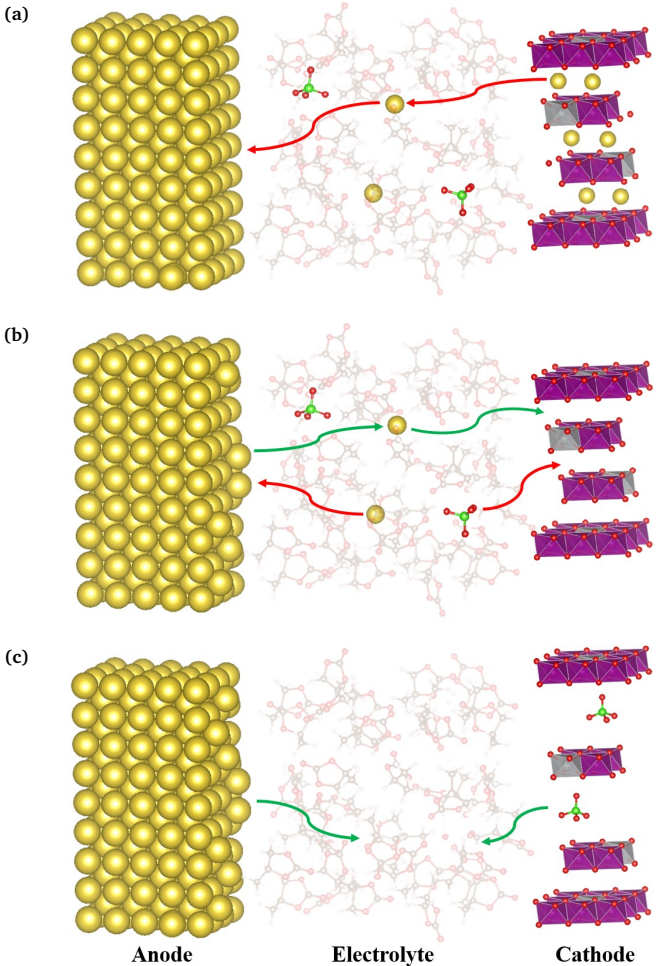


Fig. 2 Structural models of the anode, electrolyte, and cathode for different stages of the initially investigated charging mechanism of full desodiation followed by perchlorate intercalation. This charging "path" (i.e., $(a)\rightarrow (b)\rightarrow (c))$ is denoted with red arrows, while the discharge mechanism $((c)\rightarrow(b)\rightarrow(a))$ is shown with green arrows.

2.6 Charge Compensation Reactions

During the charging cycle of NMO, charge compensation reactions involving cationic (Ni²⁺ \leftrightarrow Ni⁴⁺) and anionic (O²⁻ \leftrightarrow O⁻) redox reactions have been shown to occur 25. Therefore, the ability to computationally capture and accurately model these reactions is of particular interest in this work. To investigate these proposed reactions, DOS, oxidation state determination through the use of the density derived electrostatic and chemical (DDEC6) charges approach 91-99 in conjunction with ligand field theory 100, Bader charge analysis, and structural deformations (i.e., changes in X– O bond lengths, where X = Mn, Ni, O) are all computed to determine the computational validity of these charge compensation mechanisms.

3 Results

3.1 Structural Characterization

As stated in Sec. 2.2, full structural relaxations were completed for the fully sodiated NMO structure using an assortment of xc functionals, both with and without additional vdW correction terms. The numerical results of these calculations can be found in Table S2†, with a full comparison between them and experiment 25 in Sec. S4†. In short, we conclude that the xc functional of PBE (without the inclusion of vdW corrections) yields best overall agreement. Discussion on the structural characterization for the fully perchlorated structure can also be found in Sec. S4†, with additional anion intercalation investigations discussed in Sec. S5†.

3.2 Ion Migration Barriers

Diffusion barriers were calculated for both Na and ClO₄, individually, as outlined in Sec. 2.3. A combination of four individually calculated pathways (shown in Fig. 3a & 3b for Na and ClO₄, respectively) are combined to represent ion migration throughout the NMO interlayer space. The combination of these plots is shown in Fig. 3c, where it is evident that both Na and ClO₄ are freely able to diffuse (with barriers < 0.1 eV) through the interlayer spacing of NMO; corroborating the experimental claim that both ions readily intercalate within the bulk 25 .

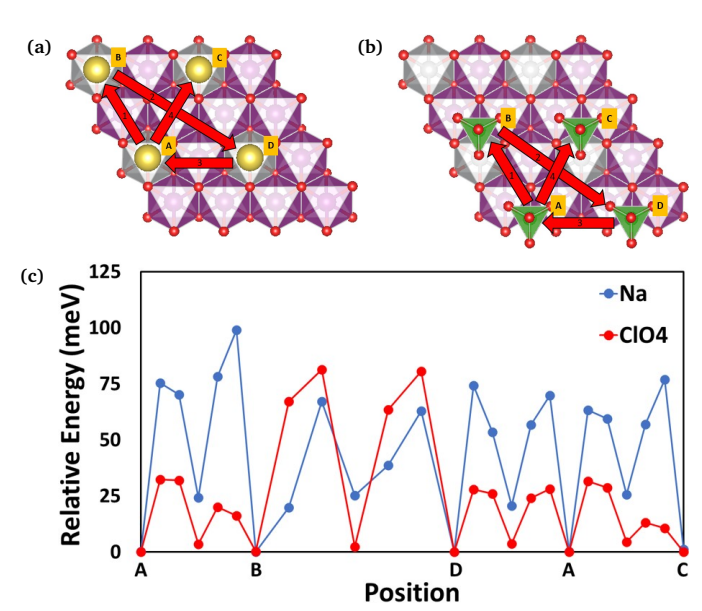


Fig. 3 The four individual migration pathways investigated for (a) Na and (b) ClO₄. The energetics of these pathways were combined following the pathway of $A \rightarrow B \rightarrow D \rightarrow A \rightarrow C$ (*i.e.*, numerical order of red arrows in (a) and (b)) to create the diffusion barrier plot in (c). For both Na and ClO₄, diffusion barriers calculated with PBE-D3 are well below the theoretically determined threshold of 0.525 eV from Rong et al. 101.

3.3 Electrochemical Performance

Due to the structural match between our calculations for Na intercalation and experiment (and how closely the empty and ClO₄intercalated structures match that of Na-intercalated for the a and b lattice vectors), only PBE-D3 was used in all voltage calculations in this work. The decision to include D3 was based on the desire to more accurately account for interactions occurring within the electrolyte simulation cells, in turn more accurately determining the voltage profile.

We began our electrochemical investigation with the process

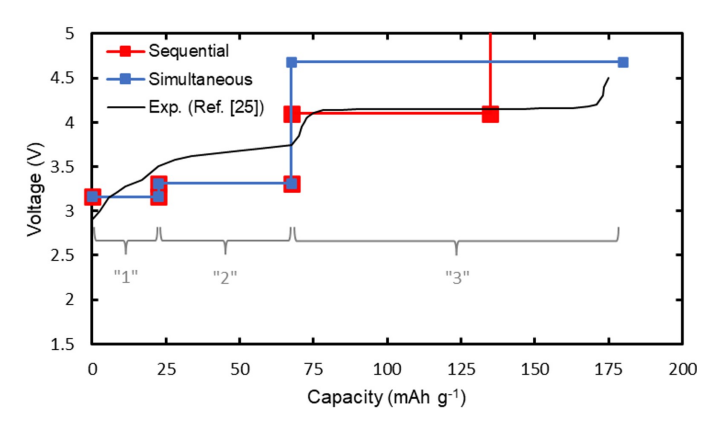


Fig. 4 Voltage profiles for charging NMO from $Na_{0.5}Ni_{0.25}Mn_{0.75}O_2$ to $Ni_{0.25}Mn_{0.75}O_2$ (ClO₄)_{0.167} for this work are shown as red and blue lines, which are discussed in Sec. 3.3. The reported voltage profile of Li *et al.* ²⁵ has been adapted and included as a black line. Also labeled are the three distinct charging plateaus.

of full desodiation followed by perchlorate intercalation, as was the suggested mechanism reported by Li *et al.* ²⁵. Their reported voltage profile (which was adapted and included in Fig. 4 as a black line) consists of three distinct plateaus during charging. These plateaus approximately run from 0–22, 22–67, and 67–180 mAh g⁻¹, respectively, and are labeled on Fig. 4. In their analyses (*e.g.*, Field-Emission Transmission Electron Microscopy and X-ray Diffraction), Li *et al.* demonstrated the NMO cathode contained only Na cations when discharged and only ClO₄ anions when charged. These two end points of charging correspond to our fully sodiated and fully perchlorated structures (shown in Fig. 1a & 1c, respectively). It is the middle region (*i.e.*, partially charged) that is the focus of this investigation as it was not comprehensively characterized previously.

For the desodiation process, formation energies were determined and a corresponding convex hull (Fig. S7†) was constructed. Next, a voltage profile (red data points in Fig. 4) was created utilizing Eqn. 3 for those points residing on the convex hull. Complete desodiation corresponds to the voltage profile from 0 to 134 mAh g $^{-1}$. From the empty NMO structure, ClO₄ intercalation was then simulated. The voltages were calculated for a variety of simulated systems, as discussed in Sec. 2.4 & 2.5. All voltages obtained for charging from empty NMO to ClO₄-intercalated are shown in Table S4†. All of those voltages are well above the experimentally reported 25 value of \sim 4.15 V for the third charging plateau, with some values as high as 6 V. The resulting voltage profile for the combination of sequential desodiation and subsequent perchloration is shown as the red line Fig. 4.

From Fig. 4, we noticed how the first two plateaus are of appropriate width (*i.e.*, capacity range), despite the fact they are an underestimation of the experimental voltage. Due to the discrep-

ancy between calculated and experimental voltage, one needs to consider the validity of Eqn. 3. However, we are confident in this method as it has provided excellent agreement to experiment in previous works 11,12,15,16,102,103 . The third plateau, however, is broken when following the process of full desodiation and then perchloration such that the voltage corresponding to perchlorate intercalation into empty NMO is well above the experimentally reported value. Therefore, we propose an alternative mechanism to that of Li *et al.* 25 in which the sequence of cation deintercalation/anion intercalation is investigated.

Our electrochemical investigation shifted to the possibility and plausibility of a charging mechanism that was not sequential in nature. That is, one in which cation deintercalation and anion intercalation was occurring simultaneously. As one potential mechanism, the first two plateaus are kept the same as the sequential mechanism (i.e., $6 \rightarrow 5 \rightarrow 3$ Na ions, for our supercell). At this partially charged state, half of the total Na has been removed. Then, in one simultaneous step, the remaining Na is to be removed while all of the ClO_4 is inserted. However, in order to calculate the voltage for this new mechanism, we need to revisit Eqn. 4.

Here, we propose a modification to the constituents included in the charged and discharged states. For a simultaneous mechanism, there may exist Na and ClO₄ within our cathode at the start and end of a given charging step. As such, Eqn. 4 requires modification to account for this possibility. We therefore present Eqn. 5 below. Here, all terms are defined as before. Now, y and j (x and i) are the number of Na and ClO₄ units, respectively, within the charged (discharged) cathode. Similarly, β (α) is the number of salt pairs within the charged (discharged) electrolyte. These two new variables are taken as $\{\alpha, \beta\} = \{3, 2\}$ and $\{2, 1\}$, with corresponding voltages calculated for both sets and averaged. This is done to simulate the voltage around the average of 2 salt pairs in our simulated electrolyte, which corresponds to a 1M concentration (as used by Li et al. 25 and shown in Table S1†). Additionally, $\gamma = (x - y) + (j - i)$, which equates to the number of electrons transferred within the charging reaction shown in Eqn. 6 below. If an investigated charging step involves a process such that (j-i)=2 (i.e., the largest value it can have for our simulation cell), then a single voltage is calculated for $\{\alpha, \beta\} = \{3, 1\}$; this again keeps the 1M average for electrolyte molarity. If (j-i)=0(i.e., only Na deintercalation occurs), then $\alpha = \beta$ and those terms are dropped from Eqn. 5. Utilizing our new equation, we are now able to compute the voltage of our initially proposed simultaneous mechanism of going from partially sodiated (x = 3 and i = 0) to fully perchlorated (y = 0 and j = 2). The result of this charging mechanism is shown in Fig. 4 as a blue line, which results in a voltage profile that qualitatively matches the experimental result much better, having a continuous (i.e., unbroken) third plateau.

With this result, the proposed mechanism of simultaneous Na

$$V = \frac{\left(\gamma E_{\text{Na}} + E_{\text{NMO,yNa,}j\text{ClO}_4} + E_{24\text{PC},\beta \text{NaClO}_4}\right) - \left(E_{24\text{PC},\alpha \text{NaClO}_4} + E_{\text{NMO,xNa,}i\text{ClO}_4}\right)}{\gamma e^{-}}$$
(5)

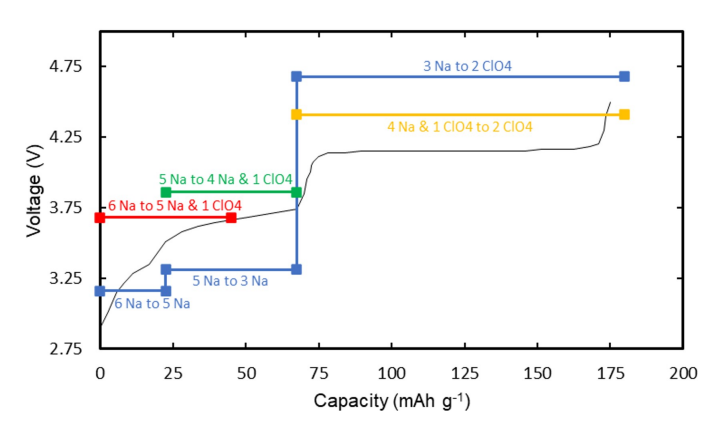


Fig. 5 A subset of some of the numerous potential steps to charge from Na $_{0.5}$ Ni $_{0.25}$ Mn $_{0.75}$ O $_{2}$ to Ni $_{0.25}$ Mn $_{0.75}$ O $_{2}$ (ClO $_{4}$) $_{0.167}$ investigated in this work. The reported voltage profile of Li *et al.* 25 has been adapted and included as a black line.

deintercalation and ClO_4 intercalation was now of great interest. A thorough search of the literature determined that the process of simultaneous cation deintercalation/anion intercalation within the same material is a novel idea with only one other work stating its possibility 104 (others have reported it for different electrodes 105). Based on this novel idea, we began investigating various pathways from fully sodiated to fully perchlorated involving several simultaneous processes. A telling, non-exhaustive, summary of these results is provided in Fig. 5.

Inspection of Fig. 5 reveals several key insights into the proposed charging mechanism for NMO. For the first charging plateau (0–22 mAh g $^{-1}$), it can be seen that Na deintercalation alone (blue line) results in a voltage mostly below that of experiment (black line). However, when coupled with simultaneous intercalation of ClO_4 (i.e., 1 molecule or half of the total amount of ClO_4 based on our simulation cell used), an increase in voltage is observed (red line). It is understood that this process does not correspond to the same capacity range for the first plateau; it is simply a consequence of the available combinations/concentrations of our simulated cells. Therefore, it is believed the actual process for this first charging step to be a mix of Na removed and ClO_4 inserted.

It is evident for the second plateau (22–67 mAh $\rm g^{-1}$) of charging that desodiation alone (blue line) yields a voltage too low yet again and that a simultaneous process (green line) yields a voltage higher than experiment. For this step, it is our belief that one-sixth of the total Na is removed from the NMO material, while one-quarter of the total $\rm ClO_4$ is inserted. It should be noted that these concentrations are based on those available within our supercell. However, we suspect the true concentrations be quite close to those proposed above.

Finally, the last (and largest) plateau of the charging process (67–180 mAh g^{-1}) demonstrates two things. First, the voltage obtained from intercalating 100% of the perchlorate (blue line)

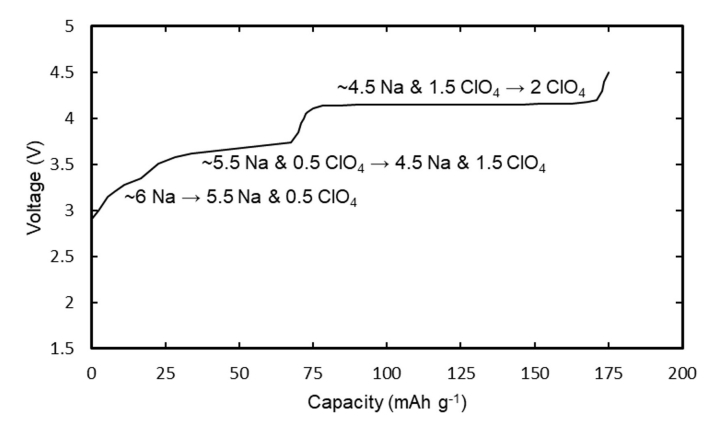


Fig. 6 The proposed mechanism for charging from Na $_{0.5}$ Ni $_{0.25}$ Mn $_{0.75}$ O $_2$ to Ni $_{0.25}$ Mn $_{0.75}$ O $_2$ (ClO $_4$) $_{0.167}$ through simultaneous cation (Na) deintercalation and anion (ClO $_4$) intercalation for the voltage profile of Li *et al.* 25 (adapted and included as a black line). NOTE: The number of each ion represented here is based on those concentrations available with the simulation cells utilized in this work.

or the remaining 50% of the perchlorate (after 50% of the perchlorate is already interclated; yellow line) resulted in voltages that are too high (by 0.53 V and 0.26 V, respectively). Secondly, the voltage obtained when more Na is removed and less ${\rm ClO_4}$ is inserted yields better agreement with experiment (i.e., the yellow line compared to the blue line).

Based on the previously discussed steps, we propose the actual charging mechanism for NMO from fully sodiated to fully perchlorated is that as shown in Fig. 6, in which we have adapted and included the reported voltage profile from Li *et al.* ²⁵. It would be ideal to compute the voltage for the proposed dual ion concentrations presented in Fig. 6. However, such concentrations require simulation cells beyond what could be handled with the available computational resources. It is to the best of our knowledge that this proposed mechanism is the first account of a computational claim of simultaneous cation deintercalation/anion intercalation within the same cathode material. With this newly proposed charging mechanism, and the previous claims of redox charge compensation reactions, we turn our investigation to determine how NMO electronically responds to each of these intercalated ions.

3.4 Charge Compensation Response of NMO

The following investigations and analyses are completed for the fully sodiated to empty to perchlorated charging mechanism, in apparent contradiction with our proposed mechanism in the previous section. However, the choice to investigate the following methods in this manner was deliberate to isolate the effects of cation deintercalation from those of anion intercalation, allowing us to determine which ion plays the major contributing role in the charge compensation reactions proposed. As discussed in Sec. 2.1, all charge compensation investigations utilize the PBE-

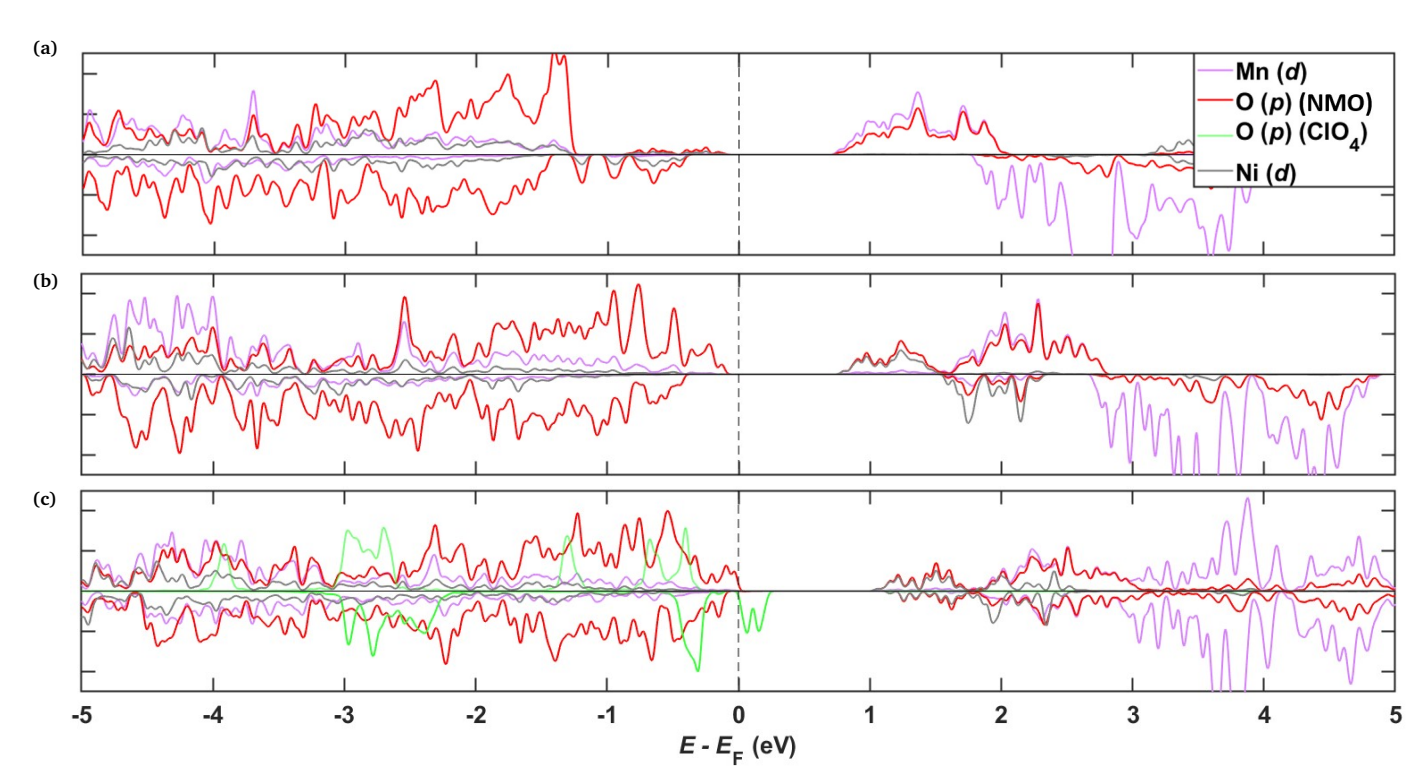


Fig. 7 Atom-resolved density of states (PDOS) for (a) $Na_{0.5}Ni_{0.25}Mn_{0.75}O_2$, (b) $Ni_{0.25}Mn_{0.75}O_2$, and (c) $Ni_{0.25}Mn_{0.75}O_2$ (ClO₄)_{0.167}. Each of these plots was calculated using PBE-D3+ U. NMO oxygens have been separately plotted from those of ClO₄ in plot (c). The Fermi level is indicated by the vertical dashed lines.

D3+U combination for their respective calculations.

3.4.1 Density of States

We begin with the electronic structure of the fully sodiated NMO system. As shown in Fig. 7a, there is a high level of hybridization between the TM(d) states and O(p) states. Such hybridization indicates a strong covalent character of the TM–O bonds 106 . Consequently, this indicates O redox is more likely to occur than TM redox 107 . When inspecting the states slightly below the Fermi level (-1 $\leq E - E_{\rm F} \leq$ 0), one can see that mainly O(p) and Ni(d) states contribute to these energies. As such, one would expect the Ni–O bonds to be the redox active centers during desodiation 46 .

In the electronic structure of empty NMO (Fig. 7b), a drastic increase in contributions from O(p) states can be seen just below the Fermi level. This shift to higher energies is indicative of O atoms compensating for the charge removed during cation deintercalation, as previously reported $^{46,49,50,106-110}$. Concurrent with this change, Ni(d) states have emptied and shifted to the conduction band (around 1 to 2 eV), indicating Ni atoms are compensating for charge removal during cation deintercalation 46,47,50,108,110,111 .

Lastly, Fig. 7c presents the electronic structure of the fully perchlorated structure. From the claim of Li *et al.* 25 , and others in literature $^{46,47,50,106-109}$, it was expected to see further redox activity of O(p) states. Comparing Fig. 7c to Fig. 7b, one can see that no significant change in any Ni, Mn, or lattice O atoms occurs. However, there is interesting behavior of the O atoms contained within ClO₄. For these states, we see high levels of hy-

bridization with all other atoms throughout the displayed energy range, as well as significant contribution to those states near the Fermi level; behaviors indicative of some level of redox activity.

Throughout the charging process, the character of the $\mathrm{Mn}(d)$ states remains unchanged, indicating that Mn takes no part in any redox reactions present in our system. This is expected as further oxidation of Mn^{4+} to Mn^{5+} is highly unfavorable energetically for Mn atoms in octahedral coordination geometries. Although a small increase in Mn character can be seen just below the Fermi level during desodiation, we attribute this to lattice O coordinated with Mn undergoing redox. As the $\mathrm{TM}(d)$ and $\mathrm{O}(p)$ states are strongly hybridized, this change is Mn character is not unreasonable. As such, the PDOS of Mn throughout the charging process are deemed to be the typical charge order of Mn^{4+} .

From our electronic structure investigation for the fully sodiated, empty, and fully perchlorated systems, we conclude that Mn atoms within all systems maintains a Mn⁴⁺ oxidation state. For the desodiation portion of the charging process, clear changes in electronic character of Ni(d) and O(p) states suggests simultaneous Ni²⁺ \rightarrow Ni⁴⁺ and O²⁻ \rightarrow O⁻ transitions. Additionally, it would appear the O atoms on ClO₄ experience some nature of redox. However, further investigation into this intriguing observation is necessary prior to any definitive claims of such redox activity. To corroborate our other redox activity findings, we move to investigate the electronic nature of all atoms by their net magnetization through the use of the DDEC6 method.

3.4.2 DDEC6

To further examine the oxidation state of Ni, Mn, and O atoms in our fully sodiated, empty, and fully perchlorated NMO systems, we calculated the net spin moments on all atoms following the DDEC6 method 91-99. However, the net spin moment is insufficient to determine oxidation state on its own. One must follow ligand field theory 100 (the more accurate modification of crystal field theory 112,113) to take this spin moment and determine the oxidation state it corresponds to 49,50,106–108,111. A description of this process is given in Sec. S7†, where electronic configurations for Ni and Mn are presented in Fig. S8 & S9†, respectively. From these electronic configurations, we expect to obtain a value of 3 μ_B for a Mn⁴⁺ oxidation state, and a value of 2/0 μ_B for a Ni²⁺/Ni⁴⁺ oxidation state. However, it has been reported ¹¹¹ that these numbers may be closer to 2.75 μ_B for a Mn⁴⁺ and 1.5 μ_B for Ni^{2+} due to the TM(d) and O(p) orbital hybridization discussed in Sec. 3.4.1.

The results of all net spin moment determinations are presented in Fig. 8. To start, we focus on Mn in the fully sodiated and empty NMO structures. Here, the Mn atoms average a net spin moment of 3.24 and 3.26 μ_B , respectively, matching a previously reported value ¹⁰⁶. Moving to the perchlorated system, we see a slight increase (3.4 μ_B). As with the PDOS of Sec. 3.4.1, this slight change could be attributed to the coordinated O atoms' redox activity and is unlikely an indication of a shift towards Mn⁵⁺ due to the energetic favorability of Mn⁴⁺ in the octahedral geometry.

For Ni atoms, there is a clear change from the ${\rm Ni}^{2+}$ oxidation state to that of ${\rm Ni}^{4+}$ during desodiation, with a further decrease in net spin moment during perchlorate intercalation. However, like those changes for Mn, these variations for Ni during perchlorate intercalation are minimal, most likely due to coordinated O redox activity, and the corresponding values match those previously reported 106 .

Although ligand field theory is not applied, the net spin moments for O atoms were investigated for sake of completeness and are included on Fig. 8 as well. For both desodiation and perchlorate intercalation, there are negligible changes. The reason no change in net spin moment is found for O is likely due to the hy-

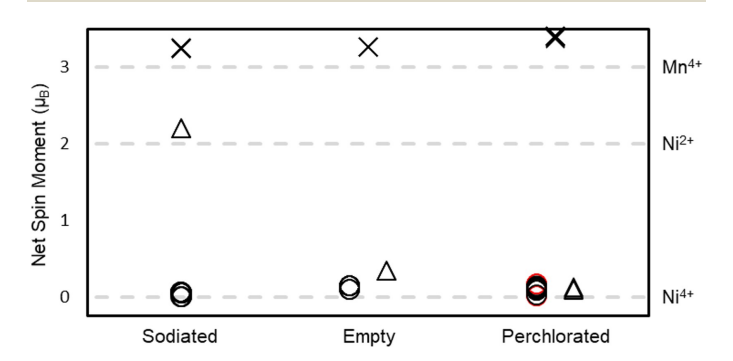


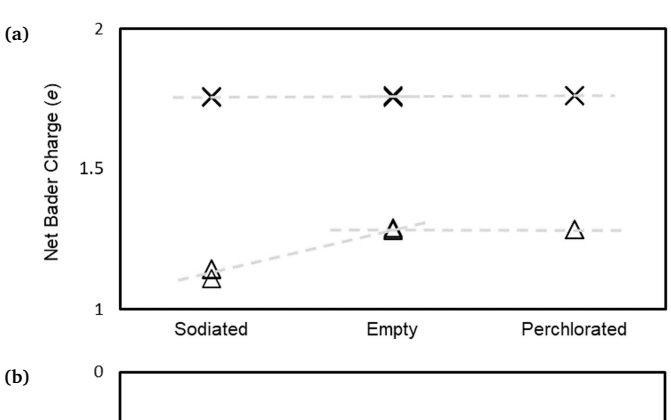
Fig. 8 Net spin moments for Ni (\triangle) , Mn (\times) , and O (\bigcirc) atoms in fully sodiated, empty, and fully perchlorated NMO when calculated with PBE-D3+U. Shown on the right are the corresponding oxidation states for the Ni and Mn atoms. The red circles for the fully perchlorated system denote oxygen atoms within ClO₄.

bridization of the TM(d) and O(p) states and choice of functional combination. Any changes that do occur for O are overshadowed by the drastic changes occurring on the Ni atoms. Additionally, electrons from neighboring atoms could be captured with the inclusion of the D3 correction, effectively canceling out any spin moments on O (as well as leading to the overestimation for Mn and Ni atoms).

Thus far, PDOS and net spin moments have been investigated to find evidence of charge compensation redox reactions. What these methods highlight is that no single method should be used in the determination of electronic structure. Various methods should be used in conjunction to fully understand the underlying electronic structure and any fluctuations therein. To this end, we move to further investigate/corroborate the suspected charge compensation reactions of $\mathrm{Ni}^{2+} \to \mathrm{Ni}^{4+}$ and $\mathrm{O}^{2-} \to \mathrm{O}^-$, as well as the inactivity of Mn, through Bader charge analysis.

3.4.3 Bader Charge Analysis

For Bader charge analysis, we are not specifically interested in the absolute value obtained from this method. Instead, we seek to find how the quantity changes during the charging process. It is this change that will indicate potential redox activity. The calculated Bader charge for all atoms within our three systems are presented in Fig. 9. To accentuate any changes that occur in the data, Fig. 9a & 9b zoom in on the Ni/Mn and O Bader charges, respectively. For both plots, two dashed lines represent linear fits for subsets of the data. One subset is the fully sodiated and empty systems, the other being those data for the empty and fully perchlorated systems.



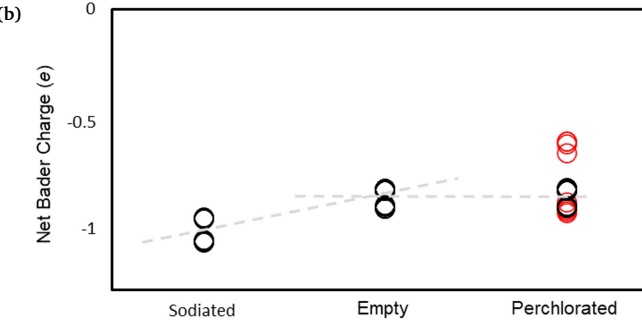


Fig. 9 Bader charge analysis for (a) Ni (\triangle), Mn (\times), and (b) O (\bigcirc) atoms in fully sodiated, empty, and fully perchlorated NMO when calculated with PBE-D3+U. The red circles for the fully perchlorated system in (b) denote the oxygen atoms within ClO₄. Also shown are linear-fits (discussed in Sec. 3.4.3) to accentuate changes.

In Fig. 9a, Mn maintains a consistent value across all stages of charging. For Ni, however, a clear discontinuity occurs at the empty NMO system. For desodiation, a change of $\sim 0.16e$ occurs on Ni atoms, which matches changes others have previously reported for similar systems 49,106 . It should be noted that such a change (specifically, a change < 0.2e) has been reported as insignificant 106 . However, in combination with the PDOS and net spin moments previously discussed, we believe this small change to be further evidence for the Ni²⁺ \rightarrow Ni⁴⁺ transition. Upon further charging, Ni atoms experience no additional change.

For O atoms, Fig. 9b illustrates several interesting points. First, as with Ni, we can see a change (\sim 0.2e) occur for the desodiation process and no change for perchlorate intercalation. Although such a change has been previously reported as insignificant ¹⁰⁶, combining this change with those observations in the PDOS corroborates a O²⁻ \rightarrow O⁻ transition. As previously discussed for the PDOS in Sec. 3.4.1, Fig. 9b shows O atoms within ClO₄ exhibiting interesting behavior. For some of these atoms (which are denoted by the red circles), the calculated Bader charge seemingly demonstrates further redox activity. However, this is difficult to determine as the ClO₄ O's have no previous values to compare to; their Bader charges may simply be the result of computational artifacts and should not be taken as claim of redox activity.

As previously stated, utilizing a single method is not sufficient for investigating charge compensation redox reactions, as evident by the minimal change in Bader charge for Ni and O atoms. While PDOS, the DDEC6 method, and Bader charge analysis provide insight into the electronic nature of a material, sometimes a simple structural analysis can prove insightful as well. Therefore, the changes in various X–O (X = Mn, Ni, O) bonds were investigated for structural (octahedron) distortions as evidence of redox activity.

3.4.4 X-O Bond Changes

As structural distortions (*i.e.*, bond length changes) have been previously reported as evidence of redox activity 46,49,106,107,109,114,115 , we include such a method to complement the electronic structure analyses from Sec. 3.4.1–3.4.3 and conclude our investigation of the charge compensation response of NMO. To accomplish this, the radial distribution function, g(r), was individually determined for Mn–O, Ni–O, and O–O bonds with the Open Visualization Tool (OVITO) 116 . Each of these bond types are separately plotted for the fully sodiated, empty, and fully perchlorated systems.

The Mn–O and Ni–O bonds are shown in Fig. 10a & 10b, respectively. These two bond types are discussed most succinctly. The Mn–O bonds show no change throughout charging, indicative of no redox activity for these atoms. Conversely, the Ni–O bonds show a distinct shortening during desodiation and no change for perchlorate intercalation, indicating redox activity of these atoms during desodiation. These results further corroborate those previously discussed.

The O–O bond changes are shown in Fig. 11. While a great deal is shown, we will break down the changes based on our categorization of these bonds, which are all shown individually in Sec. S8†. As with the Mn–O and Ni–O bonds, O–O bonds show

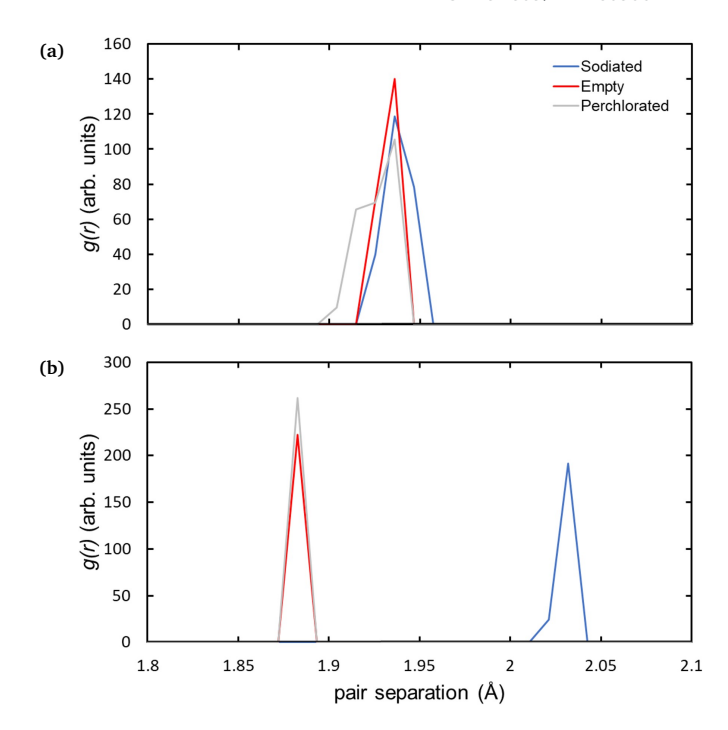


Fig. 10 Radial distribution, g(r), plots of (a) Mn–O and (b) Ni–O bonds within the fully sodiated, empty, and fully perchlorated structures when relaxed with PBE-D3+ $\it U$.

no change during charging from empty to fully perchlorated (*i.e.*, red and gray lines, respectively, in Fig. 11). Therefore, the following discussion refers exclusively to the desodiation process.

We first focus on the black arrow in Fig. 11, which points to the peaks (\sim 2.5 & 2.7 Å) corresponding to O atoms diagonal from one another in the NiO $_6$ octahedra (Fig. S10a†). These bonds shorten from 2.7 to 2.5 Å during desodiation. Similarly, O atoms within the same plane of the NiO $_6$ octahedra (Fig. S10b†) experience a shortening from \sim 3.05 to 2.8 Å (denoted by green arrows). As these two O–O bond types shorten within the NiO $_6$ octahedra, a bond type within the MnO $_6$ octahedra must lengthen to compensate. This is shown by the purple arrows, which correspond

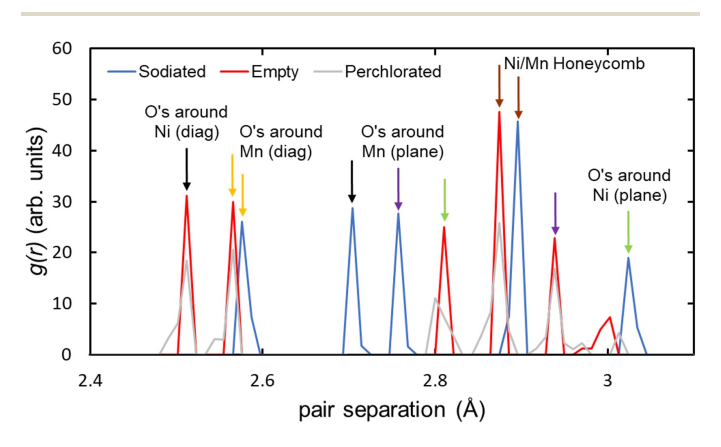


Fig. 11 Radial distribution plots of O–O bonds within the fully sodiated, empty, and fully perchlorated structures when relaxed with PBE-D3+U. Included are colored arrows denoting peaks corresponding to the same type of O atoms across the different systems (see Sec. S8† for figures of the classifications of O atoms).

to O atoms in the same plane around Mn (Fig. S10c†). Those investigated bond types which experienced no significant change are O atoms diagonally around Mn atoms (orange arrows) and those we coined as "honeycomb" (brown arrows); both of these are shown in Fig. S10d and Fig. S10e†, respectively.

Taking these data into consideration, it is evident the Mn-O bonds experience minimal change in length. Based on this, we would expect no redox activity for Mn or O (at least for those coordinated around Mn) throughout the charging process. For Ni–O bonds, a clear shortening occurs, indicating that one (or both) of the involved species undergo an electronic change during desodiation. Such a change from cation concentration alone has been shown in other investigations as well 46,49,106,107,109,114,115. The results for the Mn-O and Ni-O bond types are further corroborated through the O-O bond length investigation. Here, O atoms coordinated around Ni experience a shortening of their bonds in two different directions, providing further evidence that a concurrent redox mechanism occurs for both species. Additionally, the O atoms coordinated around Mn only experience a change in bond length as to compensate for those structural changes occurring within the neighboring NiO₆ octahedra.

Due to only investigating the sodiated and perchlorated structures (i.e., the starting and ending point for the full charging process), it is of no surprise that Li et al. 25 found evidence of Ni and O redox. However, as with the charging mechanism, we propose it is in actuality a simultaneous occurrence. As such, one may ask what then compensates for the addition of charge during perchlorate intercalation. An intriguing observation within our DOS and Bader charge calculations was that the O atoms within ClO₄ appear to become oxidized upon intercalation. However, the definitive claim of ClO₄ redox activity cannot be made without further analysis, which remains to be carried out in future work. This is where we further believe a simultaneous charging mechanism occurs, leading to no independent charge compensation required for anion intercalation as such a process does not occur on its own; Ni and O atoms undergo redox throughout the charging mechanism solely due to cation involvement.

Conclusion

Published on 27 July 2022. Downloaded on 8/31/2022 3:59:13 AM

Through our computational investigation of Na deintercalation and ClO₄ intercalation within the Ni_{0.25}Mn_{0.75}O₂ cathode material, several key insights were uncovered. First, we proposed a novel method for computationally determining the voltage associated with anion intercalation. While other methods exist for determining the voltage from anion intercalation, ours is the first to fully account for all solvent/salt interactions within the electrolyte. Through this novel method, voltages were calculated for a variety of pathways to charge from Na_{0.5}Ni_{0.25}Mn_{0.75}O₂ to $Ni_{0.25}Mn_{0.75}O_{2}(ClO_{4})_{0.167}$. It was determined that a novel simultaneous cation (Na) deintercalation and anion (ClO₄) intercalation charging mechanism occurs within this material, providing an alternative interpretation to previous reports. A major contribution to this charging mechanism of Ni_{0.25}Mn_{0.75}O₂ is the charge compensation redox reactions of Ni²⁺ \rightarrow Ni⁴⁺ and O²⁻ \rightarrow O⁻. Evidence of both oxidation state transitions was found through plotting of density of states, determination of net atomic spin moments, Bader charge analyses, and changes to X-O (X = Mn, Ni, O) bond lengths leading to structural distortions. However, our calculations show that these reactions occur simultaneously as a result of cation deintercalation and not due to anion intercalation.

In order to meet the ever-growing demand for batteries, it is essential to develop a toolkit from which we can select the nextgeneration batteries. In recent years, we have seen great advancements in building our battery toolkit with solid-state batteries, multivalent ion batteries, Li-air batteries, sulfur batteries, and beyond. In this study, we show that simultaneous dual-ion charging is a characteristic that can enhance battery performance and should be included in our growing repository of next-generation batteries.

Conflicts of interest

There are no conflicts to declare.

Acknowledgements

This work was supported by the National Science Foundation under grant number CBET-2028722. The calculations were performed using the Expanse computing cluster, a part of the Extreme Science and Engineering Discovery Environment (XSEDE, supported by National Science Foundation grant number ACI-1548562) under the allocation TG-DMR180009, as well as the Spiedie high-performance computing cluster at Binghamton Uni-

Notes and references

- 1 USP4668595, (1985); A. Yoshino, K. Sanechika, Nakajima, JP1989293, (1985).
- 2 M. S. Whittingham, Science, 1976, 192, 1126–1127.
- 3 H. Ikeda, T. Saito and H. Tamaru, Denki Kagaki, 1977, 45, 314-318.
- 4 H. Ikeda, T. Saito and H. Tamaru, Denki Kagaku, 1977, 45,
- 5 EP17400B1, (1979); Goodenough, J. B. and Mizushima, K. and Wiseman, P. J.
- 6 K. Mizushima, P. Jones, P. Wiseman and J. Goodenough, Mater. Res. Bull., 1980, 15, 783-789.
- 7 R. Yazami and P. Tauzain, J. Power Sources, 1983, 9, 365-
- 8 R. Van Noorden, Nature, 2014, 507, 26-28.
- 9 M. S. Whittingham, Chem. Rev., 2004, 104, 4271–4301.
- 10 M. S. Whittingham, MRS Bull., 2008, 33, 411-419.
- 11 T. R. Juran and M. Smeu, Phys. Chem. Chem. Phys., 2017, **19**, 20684–20690.
- 12 T. R. Juran, J. Young and M. Smeu, J. Phys. Chem. C, 2018, 122, 8788-7895.
- 13 J. Young and M. Smeu, J. Phys. Chem. Lett., 2018, 9, 3295-3300.
- 14 J. Young, P. M. Kulick, T. R. Juran and M. Smeu, ACS Appl. Energy Mater., 2019, 2, 1676–1684.
- 15 T. R. Juran and M. Smeu, J. Power Sources, 2019, 436, 226813.

View Article Online DOI: 10.1039/D2TA03938A

- 16 R. Shepard and M. Smeu, J. Power Sources, 2020, 472, 228096.
- 17 D. R. Lide, CRC Handbook of Chemistry and Physics, CRC Press, Boca Raton, Florida, 85th edn, 2005.
- 18 E. A. Olivetti, G. Cedar, G. G. Gaustad and X. Fu, Joule, 2017, 1, 229-243.
- 19 N. A. Chernova, M. Roppolo, A. C. Dillon and M. S. Whittingham, J. Mater. Chem., 2009, 19, 2526-2552.
- 20 S. P. Ong, V. L. Chevrier, G. Hautier, A. Jain, C. Moore, S. Kim, X. Ma and G. Ceder, Energy Environ. Sci., 2011, 4, 3680-3688.
- 21 M. S. Islam and C. A. J. Fisher, Chem. Soc. Rev., 2014, 43, 185-204.
- 22 P. Canepa, G. S. Gautam, D. C. Hannah, R. Malik, M. Liu, K. G. Gallagher, K. A. Persson and G. Ceder, Chem. Rev., 2017, 117, 4287-4341.
- 23 J. Ding, Y.-C. Lin, J. Liu, J. Rana, H. Zhang, H. Zhou, I.-H. Chu, K. M. Wiaderek, F. Omenya, N. A. Chernova, K. W. Chapman, L. F. J. Piper, S. P. Ong and M. S. Whittingham, Adv. Energy Mater., 2018, 8, 1800221.
- 24 J.-Y. Hwang, S.-T. Myung and Y.-K. Sun, Chem. Soc. Rev., 2017, **46**, 3529–3614.
- 25 Q. Li, Y. Qiao, S. Guo, K. Jiang, Q. Li, J. Wu and H. Zhou, Joule, 2018, 2, 1134–1145.
- 26 K. Tasaki, J. Phys. Chem. C, 2014, 118, 1443-1450.
- 27 E. Zhang, W. Cao, B. Wang, X. Yu, L. Wang, Z. Xu and B. Lu, Energy Storage Mater., 2018, 11, 91-99.
- 28 L. Xing, O. Borodin, G. D. Smith and W. Li, J. Phys. Chem. A, 2011, 115, 13896-13905.
- 29 Y. Terashima, K. Takeda and M. Honda, Chem. Phys., 2014, **430**, 23–28.
- 30 M. El Kazzi, I. Czekaj, E. J. Berg, P. Novák and M. A. Brown, Top. Catal., 2016, **59**, 628–634.
- 31 S. Kheirjou and A. Fattahi, J. Phys. Org. Chem., 2017, 31, e3798.
- 32 P. Hohenberg and W. Kohn, Phys. Rev., 1964, 136, B864-
- 33 W. Kohn and L. J. Sham, Phys. Rev., 1965, 140, A1133-A1138.
- 34 J. P. Perdew and A. Zunger, Phys. Rev. B, 1981, 23, 5048-5079.
- 35 S. Lundqvist N. H. March, and Theory of the Inhomogeneous Electron Gas, Plenum, New York, 1st edn, 1983.
- 36 W. Kohn, A. D. Becke and R. G. Parr, J. Phys. Chem., 1996, 100, 12974-12980.
- 37 W. Koch and M. C. Holthausen. A Chemist's Guide to Density Functional Theory, Wiley-VCH, Weinheim, 2nd edn, 2001.
- 38 K. Capelle, Braz. J. Phys., 2006, 36, 1318-1348.
- 39 J. P. Perdew, K. Burke and M. Ernzerhof, Phys. Rev. Lett., 1996, 77, 3865-3868.
- 40 J. Sun, A. Ruzsinszky and J. P. Perdew, Phys. Rev. Lett., 2015, 115, 036402.

- 41 S. Grimme, J. Antony, S. Ehrlich and H. Krieg, J. Chem. Phys., 2010, 132, 154104.
- 42 R. Sabatini, T. Gorni and S. De Gironcoli, Phys. Rev. B, 2013, 87, 041108(R).
- 43 H. Peng, Z.-H. Yang, J. Sun and J. P. Perdew, Phys. Rev. X, 2016, 6, 041005.
- 44 V. I. Anisimov, J. Zaanen and O. K. Andersen, Phys. Rev. B, 1991, 44, 943-954.
- 45 S. L. Dudarev, G. A. Botton, S. Y. Savrasov, C. J. Humphreys and A. P. Sutton, Phys. Rev. B, 1998, 57, 1505-1509.
- 46 M. Saubanère, E. McCalla, J.-M. Tarascon and M.-L. Doublet, Energy Environ. Sci., 2016, 9, 984-991.
- 47 P. E. Pearce, A. J. Perez, G. Rousse and M. Saubanere, Nature Mater., 2017, 16, 580-586.
- 48 J. Zheng, G. Teng, J. Yang, M. Xu, Q. Yao, Z. Zhuo, W. Yang, Q. Liu and F. Pan, J. Phys. Chem. Lett., 2018, 9, 6262-6268.
- 49 D. Kim and J. Lee, Chem. Mater., 2020, **32**, 5541–5549.
- 50 W. Zuo, F. Ren, Q. Li and X. Wu, Nano Energy, 2020, 78, 105285.
- 51 G. Kresse and J. Furthmüller, Phys. Rev. B, 1996, 54, 11169-11186.
- 52 P. E. Blöchl, Phys. Rev. B, 1994, 50, 17953-17979.
- 53 H. J. Monkhorst and J. D. Pack, Phys. Rev. B, 1976, 13, 5188-5192.
- 54 M. Methfessel and A. T. Paxton, Phys. Rev. B, 1989, 40, 3616-3621.
- 55 P. E. Blöchl, O. Jepsen and O. K. Andersen, Phys. Rev. B, 1994, 49, 16223-16233.
- 56 W. H. Press, S. A. Teukolsky, W. T. Vetterling and B. P. Flan-Numerical Recipes: The Art of Scientific Computing, Cambridge University Press, New York, 3rd edn, 2007.
- 57 K. Momma and F. Izumi, J. Appl. Crystallogr., 2011, 44, 1272-1276.
- 58 G. Mills and H. Jónsson, Phys. Rev. Lett., 1994, 72, 1124-1127.
- 59 G. Mills, H. Jónsson and G. K. Schenter, Surf. Sci., 1995, **324**, 305-337.
- 60 G. Henkelman and H. Jónsson, J. Chem. Phys., 2000, 113, 9978-9985.
- 61 G. Henkelman and H. Jónsson, Phys. Rev. Lett., 2001, 86, 664-667.
- 62 G. Henkelman, G. Jóhannsesson and H. Jónsson, Schwartz S. D. (eds) Theoretical Methods in Condensed Phase Chemistry. Progress in Theoretical Chemistry and Physics, Springer, Dordrecht, 2002, vol. 5, pp. 269-302.
- 63 D. Sheppard, R. Terrell and G. Henkelman, J. Chem. Phys., 2008, 128, 134106.
- 64 D. Sheppard and G. Henkelman, J. Comput. Chem., 2011, **32**, 1769–1771.
- 65 D. Sheppard, P. Xiao, W. Chemelewski, D. D. Johnson and G. Henkelman, J. Chem. Phys., 2012, 136, 074103.
- 66 R. Car and M. Parrinello, Phys. Rev. Lett., 1985, 55, 2471-2474.

- 67 R. Car and M. Parrinello, Phy. Rev. Lett., 1988, 60, 204-207.
- 68 K. Laasonen, R. Car, C. Lee and D. Vanderbilt, Phys. Rev. B, 1991, 43, 6796-6799.
- 69 G. Pastore, E. Smargiassi and F. Buda, Phys. Rev. A, 1991, **44**, 6334–6347.
- 70 Propylene Carbonate; MSDS No. 310328 [Online]; Sigma-Aldrich Inc.: St. Louis, MO, Nov 20, 2020.
- 71 K. Kuratani, N. Uemura, H. Senoh, H. T. Takeshita and T. Kiyobayashi, J. Power Sources, 2013, 223, 175-182.
- 72 S. Nosé, J. Chem. Phys., 1984, 81, 511-519.
- 73 W. G. Hoover, Phys. Rev. A, 1985, 31, 1695–1697.
- 74 S. Nosé, Prog. Theor. Phys. Suppl., 1991, 103, 1-46.
- 75 D. Frenkel and B. Smit, Understanding Molecular Smulation: From Algorithms to Applications, Academic Press, London, 1996.
- 76 D. Frenkel and B. Smit, Understanding Molecular Simulation: From Algorithms to Applications, Academic Press, San Diego, 2nd ed., 2002.
- 77 R. K. Pathria and P. D. Beale, Statistical Mechanics, Elsevier, Boston, 3rd ed., 2011.
- 78 M. K. Aydinol, A. F. Kohan, G. Ceder, K. Cho and J. Joannopoulos, Phy. Rev. B, 1997, 56, 1354-1365.
- 79 M. K. Aydinol, A. F. Kohan and G. Ceder, J. Power Sources, 1997, 68, 664-668.
- 80 M. K. Aydinol and G. Ceder, J. Electrochem. Soc., 1997, 144, 3832-3835.
- 81 E. Deiss, A. Wokaun, J.-L. Barras, C. Daul and P. Dufek, J. Electrochem. Soc., 1997, 144, 3877-3881.
- 82 S. K. Mishra and G. Ceder, Phys. Rev. B, 1999, 59, 6120-6130.
- 83 G. Ceder and A. Van Der Ven, Electrochim. Acta, 1999, 45, 131-150.
- 84 Y. S. Meng and M. E. Arroyo-De Dompablo, Energy Environ. Sci., 2009, 2, 589-609.
- 85 P. Bhauriyal, A. Mahata and B. Pathak, Phys. Chem. Chem. Phys., 2017, 19, 7980-7989.
- 86 K. V. Kravchyk, P. Bhauriyal, L. Piveteau, C. P. Guntlin, B. Pathak and M. V. Kovalenko, Nat. Commun., 2018, 9,
- 87 S. Kumar, P. Bhauriyal and B. Pathak, J. Phys. Chem. C, 2019, 123, 23863-23871.
- 88 X. Xiao, M. Wang, J. Tu and S. Jiao, Phys. Chem. Chem. Phys., 2019, 21, 7021-7028.
- 89 H. Saini, S. Das and B. Pathak, Mater. Adv., 2020, 1, 2418-2425.
- 90 M. L. Agiorgousis, Y.-Y. Sun and S. Zhang, ACS Energy Lett., 2017, 2, 689-693.
- 91 T. A. Manz and D. S. Sholl, J. Chem. Theory Comput., 2010, 6, 2455-2468.

- 92 T. A. Manz and D. S. Sholl, J. Chem. Theory Comput., 2011, 7, 4146-4164.
- 93 T. A. Manz and D. S. Sholl, J. Chem. Theory Comput., 2012, 8, 2844-2867.
- 94 T. A. Manz and N. G. Limas, arXiv, 2015, 1-97.
- 95 T. A. Manz and N. G. Limas, RSC Adv., 2016, 6, 47771-47801.
- 96 N. G. Limas and T. A. Manz, RSC Adv., 2016, 6, 45727-45747.
- 97 T. A. Manz, RSC Adv., 2017, 7, 45552-45581.
- 98 N. G. Limas and T. A. Manz, RSC Adv., 2018, 8, 2678-2707.
- 99 T. A. Manz, T. Chen, D. J. Cole, N. G. Limas and B. Fiszbein, ChemRxiv, 2018, 1-57.
- 100 U. Müller, Inorganic Structural Chemistry, John Wiley & Sons Inc., New Jersey, 2nd edn, 2006.
- 101 Z. Rong, R. Malik, P. Canepa, G. Sai Gautam, M. Liu, A. Jain, K. Persson and G. Ceder, Chem. Mater., 2015, 27, 6016-6021
- 102 M. Woodcox, R. Shepard and M. Smeu, J. Power Sources, 2021, 516, 230620.
- 103 D. Liepinya, R. Shepard and M. Smeu, Comp. Mater. Sci., 2022, 202, 110948.
- 104 X. Qi, B. Blizanac, A. DuPasquier, P. Meister, T. Placke, M. Oljaca, J. Li and M. Winter, Phys. Chem. Chem. Phys., 2014, 16, 25306-25313.
- 105 M. Wang and Y. Tang, Adv. Energy Mater., 2018, 8, 1703320.
- 106 A. Massaro, A. B. M. noz García, P. P. Prosini, C. Gerbaldi and M. Pavone, ACS Energy Lett., 2021, 6, 2470-2480.
- 107 M. Kim, H. Kim, M. Cho and D. Kim, J. Mater. Chem. A, 2021, 9, 15179–15187.
- 108 M. D. Johannes, K. Swider-Lyons and C. T. Love, Solid State Ion., 2016, 286, 83-89.
- 109 J.-H. Park, I.-H. Ko, J. Lee and S. Park, ChemElectroChem, 2021, 8, 625-643.
- 110 G. Choi, J. Lee and D. Kim, ACS Appl. Mater. Interfaces, 2020, 12, 29203-29211.
- 111 H. Yu, Y. Qian, M. Otani and D. Tang, Energy Environ. Sci., 2014, 7, 1068-1078.
- A. Cotton and Wilkinson. Adaynced Inorganic Chemistry: A Comprehensive Text, Wiley InterScience, New York, 4th edn, 1980.
- 113 T. Saito, Inorganic Chemistry, CreateSpace Independent Publishing Platform, South Carolina, 2014.
- 114 M. B. Yahia, J. Vergnet, M. Saubanère and M.-L. Doublet, Nature Mater., 2019, 18, 496-502.
- 115 J. Vergnet, M. Saubanère, M.-L. Doublet and J.-M. Tarascon, Joule, 2020, 4, 420-434.
- 116 A. Stukowski, Modelling Simul. Mater. Sci. Eng., 2010, 18, 015012.